frame under the influence of the interatomic potential of the remaining stationary lattice. The characteristic vibration frequency obtained for bulk ZnS is 7.12 ± 1.2 THz. This value is consistent with that reported previously for bulk CdSe (*27*, *28*). In comparison, the characteristic vibration frequency for the ZnS nanoparticles is 11.6 ± 0.4 THz. Although these values cannot be simply related to the full phonon dispersion relations for ZnS, the trend clearly indicates lattice stiffening. This implies that the heat capacity of the ZnS lattice, excluding surface-bound species, is lower in nanoparticles than in equivalent bulk material.

There are several features of the nanoparticles that may be responsible for the lattice stiffening. First, the PDF analysis indicates ~1% bond length compression. Because crystalline materials show an increase in vibration frequencies with pressure (away from phase transitions), the compression will cause lattice stiffening. However, compression of this magnitude alone cannot explain the large increase in vibration frequency. The average change in bond length provides an incomplete picture because disorder within the nanoparticles leads to a large distribution of bond lengths, and all deviations from the equilibrium bond lengths may increase the vibration frequency. We thus find that structural disorder is principally responsible for the lattice stiffening.

In summary, we quantitatively determined nanoparticle crystallinity and disorder, using a PDF-based method. We found that the best description of nanoparticle structure includes bond length contraction, random disorder, and a type of disorder characterized by correlated atomic displacements. The internal disorder is observed despite the presence of strongly bound surface ligands. We conclude that even with strong chemical passivation, surface atoms exist in diverse unsatisfied bonding environments at the surface that drive inhomogeneous internal strain. A striking consequence of the internal disorder is that the nanoparticles are much stiffer than expected from the measured bond length contraction. Our approach is an important step toward a realistic description of nanoparticle structure that includes internal strain, which is likely to be a general feature of nanoscale solids. Because lattice contraction and disorder will separately modify electronic properties, inclusion of these effects is essential for accurate nanoparticle calculations.

References and Notes

1. R. Rossetti, R. Hull, J. M. Gibson, L. E. Brus, *J. Chem. Phys.* **82**, 552 (1985).
2. C. B. Murray, D. J. Norris, M. G. Bawendi, *J. Am. Chem Soc.* **115**, 8706 (1993).
3. A. P. Alivisatos, *Science* **271**, 933 (1996).
4. L. E. Brus, *J. Chem. Phys.* **80**, 4403 (1984).
5. P. E. Lippens, M. Lannoo. *Phys. Rev. B* **39**, 10935 (1989).
6. A. Franceschetti, A. Zunger, *Phys. Rev. Lett.* **78**, 915 (1997).
7. B. Palosz *et al*., *Z. Kristallogr.* **217**, 497 (2002).
8. L.-W. Wang, A. Zunger, *Phys. Rev. B* **53**, 9579 (1996).
9. K. Leung, K. B. Whaley, *J. Chem. Phys.* **110**, 11012 (1999).
10. E. Rabani, *J. Chem. Phys.* **115**, 1493 (2001).
11. A. Puzder, A. J. Williamson, F. A. Reboredo, G. Galli, *Phys. Rev. Lett.* **91**, 157405 (2003).
12. H. Zhang, B. Gilbert, F. Huang, J. F. Banfield. *Nature* **424**, 1025 (2003).
13. W. Vogel, P. H. Borse, N. Deshmukh, S. K. Kulkarni, *Langmuir* **16**, 2032 (2000).
14. See supporting online material.
15. B. J. Thijsse, *J. Appl. Crystallogr.* **17**, 61 (1984).
16. A. C. Wright *et al*., *J. Non-Cryst. Solids* **129**, 213 (1991).
17. S. J. L Billinge, M. F. Thorpe, Eds., *Local Structure from Diffraction* (Plenum, New York, 1998).
18. J. Rockenburger, *et al*. *J. Chem. Phys.* **108**, 7807 (1998).
19. M. A. Marcus, W. Flood, M. Steigerwald, L. Brus, M. Bawendi. *J. Phys. Chem.* **95**, 1572 (1991).
20. A. C. Carter, *et al*., *Phys. Rev. B* **55**, 13822 (1997).
21. M. G. Bawendi, A. R. Kortan, M. L. Seigerwald, L. E. Brus, *J. Chem. Phys.* **91**, 7282 (1989).
22. G. Mason, *Nature* **217**, 733 (1968).
23. I.-K. Jeong, Th. Proffen, F. Mohiuddin-Jacobs, S. J. L. Billinge, *J. Phys. Chem. A* **103**, 921 (1999).
24. J.-J. Shiang, A. V. Kadavanich, R. K. Grubbs, A. P. Alivisatos, A. P. 1995. *J. Phys. Chem.* **99**, 17417 (1995).
25. A. L. Ankudinov, B. Ravel, J. J. Rehr, S. D. Conradson, *Phys. Rev. B* **58**, 7565 (1998).
26. A. I. Frenkel, J. J. Rehr, *Phys. Rev B* **48**, 585 (1993).
27. G. Dalba, *et al*., *Phys. Rev. B* **58**, 4793 (1998).
28. For two atoms vibrating in their center of mass frame in an effective pair potential characterized by spring constant k, the bond frequency, $\omega = \sqrt{k/\mu}$, where μ is the reduced mass. For CdSe, $1/\mu = 1/M_{Cd} + 1/M_{Se}$ (M_{Cd} is the atomic mass of Cd). For CdSe, $\nu_{CdSe} = 4.97$ THz (*27*). For ZnS, we obtained $\nu_{ZnS} = 7.12$THz. The interatomic force constants for CdSe and ZnS are expected to be similar. If we assume that $k_{CdSe} = k_{ZnS}$, then $\left.\frac{\omega_{CdSe}}{\omega_{ZnS}}\right|_{predicted} = \sqrt{\frac{\mu_{ZnS}}{\mu_{CdSe}}} = 0.68$. In fact, $\left.\frac{\omega_{CdSe}}{\omega_{ZnS}}\right|_{observed} = \sqrt{\frac{\mu_{ZnS}}{\mu_{CdSe}}} = 0.676$. Hence, the results presented here for bulk ZnS and in (*27*) for bulk CdSe are in good agreement.
29. We thank M. Toney for discussion on PDF analysis, C. Kim for practical advice on EXAFS acquisition, and M. Zach for assistance with sample holder fabrication. SAXS data were acquired on beamline 1.4 at the Stanford Synchrotron Radiation Lab (SSRL), and we thank J. Pople. Zn K-edge EXAFS were acquired on beamline 4-3 at SSRL, and we thank M. Lattimer. WAXS data were acquired on beamline 11-ID-C at the Advanced Photon Source (APS), Argonne National Laboratory, and we thank Y. Ren and M. Beno. The U.S. Department of Energy, Office of Basic Energy Sciences, supports use of the APS (Contract No.W-31-109-Eng-38) and the SSRL (Contract No. DE-AC03-76SF00515). HRTEM was performed at the National Center for Electron Microscopy, Berkeley, CA, and we thank C. Song. Financial support for this work came from the U.S. Department of Energy, the National Science Foundation, and Lawrence Berkeley National Laboratory.

Supporting Online Material
www.sciencemag.org/cgi/content/full/1098454/DC1
Materials and Methods
Figs. S1 to S9
References

29 March 2004; accepted 22 June 2004
Published online 1 July 2004;
10.1126/science.1098454
Include this information when citing this paper.

Grain Boundary–Mediated Plasticity in Nanocrystalline Nickel

Zhiwei Shan,[1] E. A. Stach,[2] J. M. K. Wiezorek,[3] J. A. Knapp,[4] D. M. Follstaedt,[4] S. X. Mao[1]*

The plastic behavior of crystalline materials is mainly controlled by the nucleation and motion of lattice dislocations. We report in situ dynamic transmission electron microscope observations of nanocrystalline nickel films with an average grain size of about 10 nanometers, which show that grain boundary–mediated processes have become a prominent deformation mode. Additionally, trapped lattice dislocations are observed in individual grains following deformation. This change in the deformation mode arises from the grain size–dependent competition between the deformation controlled by nucleation and motion of dislocations and the deformation controlled by diffusion-assisted grain boundary processes.

The plastic deformation of coarse-grained metals at relatively low temperature is usually mediated by the nucleation and motion of dislocations. However, for nanocrystalline metals, dislocation sources and pile-ups are not expected to exist within the individual grains because of the limited grain size and the much higher fraction of grain boundary (GB) atoms (*1*–*8*). It has been proposed (*3*–*6*) that GB-mediated plasticity (e.g., GB sliding and/or grain rotation) substitutes for conventional dislocation nucleation and motion as the dominant deformation mechanism when grain sizes are reduced below a certain value. This conjecture has been supported by molecular dynamics simulations (*5*, *7*, *8*) and indirect experimental evidence (*2*, *9*). Dy-

[1]Department of Mechanical Engineering, University of Pittsburgh, 648 Benedum Hall, Pittsburgh, PA 15261, USA. [2]National Center for Electron Microscopy (NCEM), Lawrence Berkeley National Laboratory (LBNL), Berkeley, CA 94720, USA. [3]Department of Materials Science and Engineering, University of Pittsburgh, Pittsburgh, PA 15261, USA. [4]Physical and Chemical Science Center, Sandia National Laboratories (SNL), Albuquerque, NM 87185, USA.

*To whom correspondence should be addressed. E-mail: smao@engr.pitt.edu

namic in situ deformation studies (*10–13*) have been performed in the transmission electron microscope (TEM) to observe the deformation mechanisms that are active in nanocrystalline metals with grain sizes in the regime where a transition in mechanism is predicted. However, direct experimental evidence of a transition in deformation mechanisms, i.e., from a dislocation-mediated deformation to a GB-mediated deformation, has not been reported (*10–14*).

The Ni samples used in this study were synthesized by directing a high-energy pulsed KrF excimer laser onto a high-purity Ni target under vacuum with a base pressure of about 2×10^{-7} torr. The resulting Ni plasma was deposited onto a [001] NaCl substrate with a nominal thickness of 150 nm. TEM observations (Fig. 1A) indicate that the as-deposited Ni consists of roughly equiaxed grains with random orientations (inset in Fig. 1A). Statistical measurements of dark-field TEM (DFTEM) images reveal a narrow, log-normal grain size distribution, ranging from several nanometers to 23 nm with an average value ($\pm$SD) of 9.7 $\pm$ 3.9 nm (Fig. 1B). High-resolution TEM (HRTEM) shows that most grains are separated by large-angle GBs. Additional GB phases, porosity, or intergranular microcracks were not detected in these samples after deposition.

The nanocrystalline nickel films were deformed by in situ TEM tensile straining (*15*). Figure 2A is a typical DFTEM image of a Ni sample in the undeformed state. Figure 2B is the corresponding selected area diffraction pattern (SADP) before deformation. Upon straining, bright-field TEM observations showed rapid changes in contrast that occur continuously in many different grains. This has previously been identified as evidence of dislocation activity (*11*, *13*). However, our in situ DFTEM observations revealed that the deformation behavior is substantially more complex. We found many strongly diffracting features that are much larger than the initial average grain size and are formed immediately in the deformed zone upon straining (e.g., the feature marked by a white arrow is about 60 nm in diameter in Fig. 2C). The SADP from the deformed area (Fig. 2D, taken from the same region and with the same selected area aperture size as the area in Fig. 2B) exhibited fewer, asymmetrically distributed diffraction spots in each of the diffraction rings in comparison with the SADP obtained before deformation (Fig. 2B). The reduced background intensity and improved contrast in the SADP of the deformed area (Fig. 2D) indicate that the sample thinned locally during deformation. Higher magnification DFTEM micrographs revealed that the large bright features observed after deformation consist of a number of smaller grains (e.g., Fig. 2E) rather than a single large grain resulting from stress-assisted grain growth. A comparison of the undeformed state (Fig. 2, A and B) and the postdeformation state (Fig. 2, C, D, and E) indicates that groups of neighboring grains underwent an orientation change during straining and formed numerous grain agglomerates. Because of the nature of the image formation mechanism of DFTEM images (*15*), we can conclude that the smaller grains in these agglomerates exhibit essentially edge-on orientations of their {111} and/or {200} lattice planes. The schematic in Fig. 2F depicts a possible crystallographic substructure associated with an agglomerated group of grains that would be consistent with the type of contrast observed in the DFTEM micrographs after straining (Fig. 2E).

To elucidate further the mechanism responsible for the formation of the agglomerated grain regions, real-time observations were performed. Contrast changes in areas subject to high strain during in situ TEM straining experiments were recorded in the dark-field (DF) mode. The DF micrographs shown in Fig. 3 are still frames extracted from a typical dynamic sequence of images taken during the application of a single displacement pulse. The times listed on each still frame are based on the video-acquisition rate of 30 frames per second. At the beginning of this sequence, there were no grains in a strongly diffracting condition in the area indicated by the white arrow (Fig. 3A). After 1/30 of a second, a bright spot emerged from a grain about 6 nm in diameter and remained well defined in size as a single, approximately equiaxed grain until t = 0.1 s (Fig. 3B). Over the next couple of frames, a number of additional neighboring grains rotated into strongly diffracting conditions for either the {200} or {111} planes. Other nearby grains, which were in a strong diffraction condition, did not rotate out of contrast, confirming that there had been no global rotation of the specimen area and that the rotations observed at

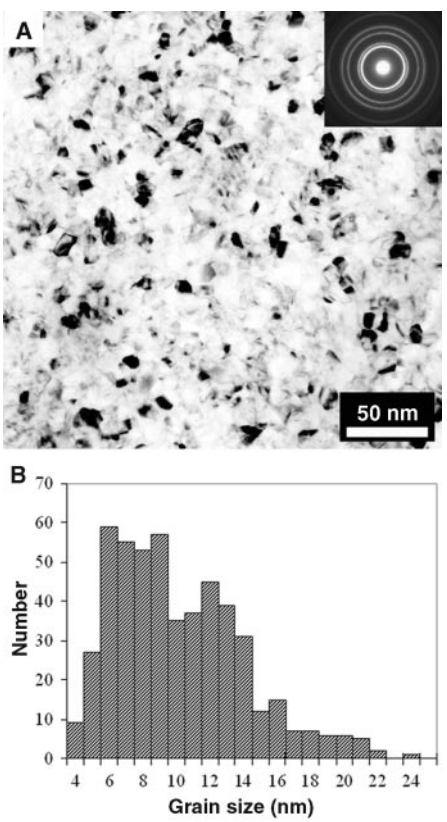

Fig. 1. TEM observations of the typical microstructure in the as-deposited nanocrystalline nickel films. The bright-field TEM micrograph (**A**) and the SADP [inset in (A)] show roughly equiaxed grains with random orientations. The statistical distributions for grain size (**B**) were obtained from multiple TEM images of the same sample.

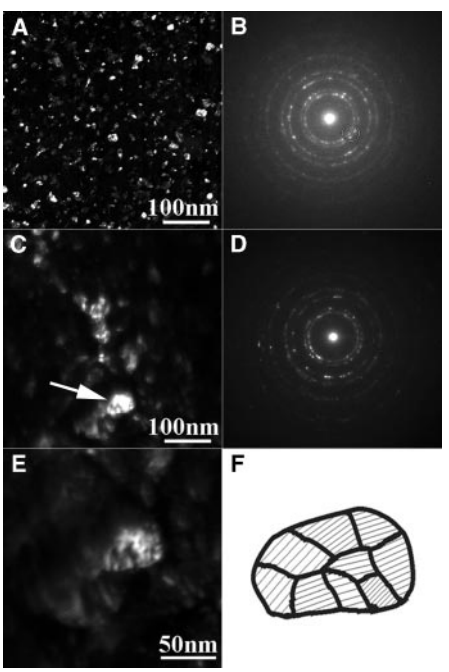

Fig. 2. TEM micrographs showing the evolution of the Ni microstructure during in situ straining. (**A**) DFTEM image of as-deposited nanocrystalline Ni film before deformation. Part of the {111} and {200} diffraction rings were selected as the image-forming diffraction vectors, as indicated schematically by the white circle in (B) (all of the DF images here are taken with this condition). (**B**) Corresponding SADP of undeformed Ni film. (**C**) DFTEM micrograph of as-deposited Ni after deformation. Features in strong diffraction contrast much larger than the average grain size are discernible (e.g., white arrow). (**D**) The corresponding SADP of the deformed Ni film. (**E**) Higher magnification DFTEM image of the feature marked by the white arrow in (C). (**F**) Schematic sketch of a possible multigrain substructure of the large features in bright contrast observed after deformation [e.g., in (C)]. The lines represent the trace of those edge-on planes.

the arrowed location were internal changes of the sample structure. Additionally, the small "notch" discernible at the lower left corner of the agglomerate (Fig. 3, D and E) indicates that the growth in size of this agglomerated group of grains was not isotropic and involved sudden rotation of individual grains. At $t = 0.5$ s, the group of grains had grown into an elongated equiaxed shape with an approximate size of 60 nm along the short axis and 80 nm along the long axis. After this very rapid morphological change, the rate of growth of the grain agglomerate decreased significantly.

These TEM observations confirm the prediction that GB-mediated deformation can become prominent when the average grain size of a material decreases below some critical value. Several theoretical studies have considered the operation of grain rotation and GB sliding as possible deformation modes (*16*–*18*). These studies assume that the driving force for grain rotation is the net torque on a grain, which results from the misorientation dependence of the energy of the GBs that delineate a given grain from its neighbors. Grain rotation is viewed as a sliding problem on the periphery of the grain; changes in the grain shape during rotation are assumed to be accommodated by diffusion, through either the GBs or the grain interiors. If GB diffusion is dominant (a reasonable assumption in nanocrystalline metals with grain size below a certain value at room temperature), it would yield a d^{-4} dependence on the rotation rate, where d is the grain size. This is a marked dependence on grain size. For example, when d is 60 and 6 nm, respectively, and all other factors are identical, the grain rotation rate for the latter will be 10^4 higher than for the former. This qualitatively explains our observation of extremely rapid formation of the grain agglomerates by rotation during straining. The rate of the grain rotation processes will generally decrease with time, as a state of new equilibrium is approached locally.

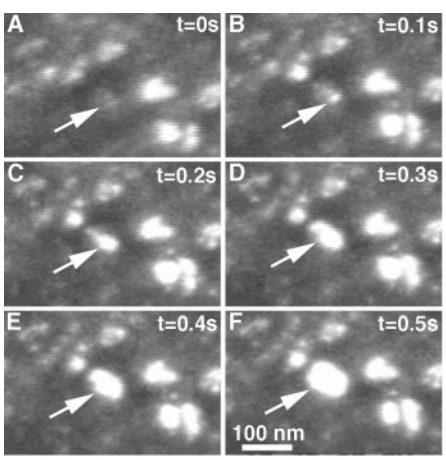

Fig. 3. DFTEM observation of the rapid genesis of an agglomerate (e.g., white arrow) depicted by individual still frames extracted from a dynamic video sequence. (**A**) At $t = 0$ s, no grains in the strong diffraction condition are near the white arrow. (**B**) At $t = 0.1$ s, a grain in the strong diffraction condition with a size of about 6 nm is visible. (**C**) At $t = 0.2$ s, a group of grains in bright contrast with a size of about 28 nm is visible. (**D**) At $t = 0.3$ s, the group of grains has a nearly elliptical shape, with dimensions of 60 by 35 nm. (**E**) At $t = 0.4$ s and (**F**) $t = 0.5$ s, the size of the group of grains increases to maximum dimensions of about 80 by 60 nm.

Previous TEM observations have indicated that dislocations may still play a role in deformation even if the average grain size falls below the grain size at which GB processes may become active (*13*). Hence, it may be expected that evidence of lattice dislocation glide activity during straining would exist in the microstructure of deformed nanostructured metals. However, detection of such evidence by postmortem TEM investigations, for instance in the form of dislocation debris or trapped lattice dislocations, has proven unsuccessful (*19*). Yamakov *et al*. (*20*) suggested that trapped dislocations may only exist inside a nanograin under very high external or internal stress and that the removal of the stress can lead to reversible reabsorption of the partial dislocations at the presumed GB source. However, the traditional sample preparation methods, such as mechanical thinning followed by ion thinning or twin jet polishing will inevitably result in some relaxation of a previously deformed microstructure. This makes it difficult to verify the assumption, and therefore limits further understanding of this important fundamental process. During this study, HRTEM images of suitably oriented grains that were still under stress were obtained in the thin area that was produced by the deformation.

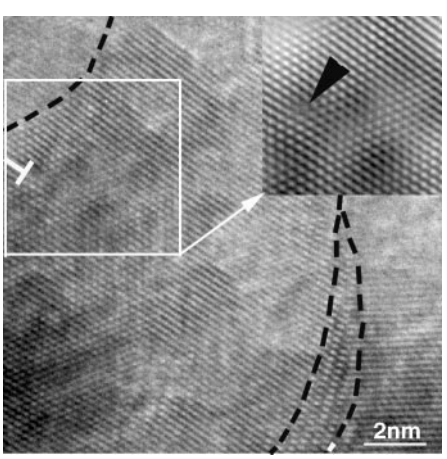

Fig. 4. A typical HRTEM image of a thin area formed by deformation. A dislocation (white T) is trapped inside a grain close to the GB (delineated by black dashed line). The inverse Fourier-filtered image (**inset**) from inside the white box shows the dislocation (black arrowhead) with more clarity.

Trapped lattice dislocations were detected in some of the grains. Figure 4 shows an example of an HRTEM micrograph of one of these trapped dislocations (white T) trapped in the vicinity of a GB (delineated by the black dashed line). The inset at the upper right corner in Fig. 4 is an inverse Fourier-filtered image of the region framed by the white box, which displays the dislocation more clearly. Local Burgers circuits were employed to determine the Burgers vectors of the dislocations in HRTEM. As for Fig. 4, the Burgers vector of the trapped dislocation was determined to be consistent with $b = \frac{a}{2}\langle 110\rangle$, where a is the lattice constant of Ni—i.e., a unit dislocation of the face-centered cubic lattice on a $(\bar{1}11)$ plane (*15*). The frequent observation of trapped lattice dislocations in the postdeformation state indicates that dislocation-mediated deformation is still active even when the average grain size is about 10 nm. Two other recent experiments have also detected the presence of dislocations in nanocrystalline Ni while under stress (*21*, *22*), although for larger grains (20 and 26 nm, respectively).

The physics governing the observed deformation crossover can be understood by considering the effect of grain size on the different operative processes. A number of computational simulations have predicted that GBs can act as dislocation sources in nanocrystalline materials (*5*, *23*, *24*). Based on these simulations, Chen *et al*. (*25*) proposed a dislocation-based model suggesting that the nucleation stress for both perfect and partial dislocations is inversely proportional to the grain size. Furthermore, this model predicts the existence of a critical grain size d_c, below which the deformation mechanism will change from one controlled by normal unit dislocation motion to one controlled by partial dislocation activity. If we take the dislocation core parameter $\alpha = 1$, the shear modulus as $\mu_{Ni} = 95$ GPa (*26*), and the stacking fault energy of nickel as ~0.128 to 0.24 J/m^2 (*27*, *28*), the critical size (d_c) for Ni then ranges from ~11 to 22 nm. However, according to this theory, the lower bound of the nucleation stress for partial dislocations (for $d = 23$ nm) in our sample is as high as ~2.1 to 2.8 GPa. This indicates that very high local stress is necessary for the nucleation of partial dislocations in nanocrystalline Ni with an average grain size of 10 nm. In contrast, the rate of GB-mediated deformation, as mentioned above, increases rapidly with a scaling of d^{-4}. Thus, the deformation mechanism crossover is an inevitable result of the competition between the deformation controlled by nucleation and motion of dislocations (unit and partial) and the deformation controlled by GB-related deformation accommodated mainly by GB diffusion with decreasing grain size.

In a critical part of our investigation, we

observed the rapid sequence of initial grain realignments by closely examining successive video frames in DFTEM mode. The frequent observation of the GB-mediated deformation reported here (Figs. 2 and 3) would not have been possible in bright-field TEM conditions because of the inherent difficulty with differentiating the contrast changes caused by GB-related deformations from those caused by the motion of lattice dislocations in small grains (e.g., less than 20 nm).

References and Notes

1. J. R. Weertman *et al.*, *Mater. Res. Soc. Bull.* **24**, 44 (1999).
2. C. C. Koch, D. G. Morris, K. Lu, A. Inoue, *Mater. Res. Soc. Bull.* **24**, 54 (1999).
3. H. Van Swygenhoven, *Science* **296**, 66 (2002).
4. J. R. Weertman, in *Nanostructured Materials: Processing, Properties and Applications*, C. C. Koch, Ed. (William Andrews Publishing, Norwich, New York, 2002), pp. 397–421.
5. J. Schiotz, F. D. DiTolla, K. W. Jacobsen, *Nature* **391**, 561 (1998).
6. S. Yip, *Nature* **391**, 532 (1998).
7. J. Schiotz, K. W. Jacobsen, *Science* **301**, 1357 (2003).
8. V. Yamakov, D. Wolf, S. R. Phillpot, A. K. Mukherjee, H. Gleiter, *Nature Mater.* **3**, 43 (2004).
9. C. A. Schuh, T. G. Nieh, T. Yamasaki, *Scripta Mater.* **46**, 735 (2002).
10. M. Ke, S. A. Hackney, W. W. Milligan, E. C. Aifantis, *Nanostructured Mater.* **5**, 689 (1995).
11. C. J. Youngdahl, J. R. Weertman, R. C. Hugo, H. H. Kung, *Scripta Mater.* **44**, 1475 (2001).
12. K. S. Kumar, S. Suresh, M. F. Chisholm, J. A. Horton, P. Wang, *Acta Mater.* **51**, 387 (2003).
13. R. C. Hugo *et al.*, *Acta Mater.* **51**, 1937 (2003).
14. H. V. Swygenhoven, J. R. Weertman, *Scripta Mater.* **49**, 625 (2003).
15. Materials and methods are available as supporting material on *Science* Online.
16. R. Raj, M. F. Ashby, *Metal. Trans.* **2**, 1113 (1971).
17. K. E. Harris, V. V. Singh, A. H. King, *Acta Mater.* **46**, 2623 (1998).
18. D. Moldovan, D. Wolf, S. R. Phillpot, *Acta Mater.* **49**, 3521 (2001).
19. M. Legros, B. R. Elliott, M. N. Rittner, J. R. Weertman, K. J. Hemker, *Philos. Mag. A* **80**, 1017 (2000).
20. V. Yamakov, D. Wolf, M. Salazar, S. R. Phillpot, H. Gleiter, *Acta Mater.* **49**, 2713 (2001).
21. R. Mitra, W.-A. Chiou, J. R. Weertman, *J. Mater. Res.* **19**, 1029 (2004).
22. Z. Budrovic, H. Van Swygenhoven, P. M. Derlet, S. V. Petegem, B. Schmitt, *Science* **304**, 273 (2004).
23. V. Yamakov, D. Wolf, S. R. Phillpot, A. K. Mukherjee, H. Gleiter, *Nature Mater.* **1**, 45 (2002).
24. H. V. Swygenhoven, P. M. Derlet, A. Hasnaoui, *Phys. Rev. B* **66**, 024101 (2002).
25. M. W. Chen *et al.*, *Science* **300**, 1275 (2003).
26. J. P. Hirth, J. Lothe, *Theory of Dislocations* (Wiley, New York, ed. 1, 1982), p. 837.
27. L. E. Murr, *Interfacial Phenomena in Metals and Alloys* (Addison Wesley, Reading, MA, 1975).
28. P. S. Dobson, P. J. Goodhew, R. E. Smallman, *Philos. Mag.* **16**, 9 (1967).

29. Supported by NSF grant CMS-0140317 to the University of Pittsburgh. The work at NCEM/LBNL and at SNL was supported by the Director, Office of Science, Office of Basic Energy Sciences, Division of Materials Sciences and Engineering, of the U.S. Department of Energy. Sandia is a multiprogram laboratory operated by Sandia Corporation, a Lockheed Martin Company, for the United States Department of Energy's National Nuclear Security Agency under contract DE-AC04-94AL85000. We thank L. Lu and C. Y. Song for fruitful discussion.

Supporting Online Material

www.sciencemag.org/cgi/content/full/305/5684/654/DC1
Materials and Methods
Fig. S1

5 April 2004; accepted 18 June 2004

Pinpointing the Source of a Lunar Meteorite: Implications for the Evolution of the Moon

Edwin Gnos,[1]* Beda A. Hofmann,[2] Ali Al-Kathiri,[1] Silvio Lorenzetti,[3] Otto Eugster,[3] Martin J. Whitehouse,[4] Igor M. Villa,[1] A. J. Timothy Jull,[5] Jost Eikenberg,[6] Bernhard Spettel,[7] Urs Krähenbühl,[8] Ian A. Franchi,[9] Richard C. Greenwood[9]

The lunar meteorite Sayh al Uhaymir 169 consists of an impact melt breccia extremely enriched with potassium, rare earth elements, and phosphorus [thorium, 32.7 parts per million (ppm); uranium, 8.6 ppm; potassium oxide, 0.54 weight percent], and adherent regolith. The isotope systematics of the meteorite record four lunar impact events at 3909 ± 13 million years ago (Ma), ~2800 Ma, ~200 Ma, and <0.34 Ma, and collision with Earth sometime after 9.7 ± 1.3 thousand years ago. With these data, we can link the impact-melt breccia to Imbrium and pinpoint the source region of the meteorite to the Lalande impact crater.

The elevated Th content of the lunar Procellarum terrane was recognized during the Apollo gamma-ray remote mapping program (*1*). The terrane, which includes Mare Imbrium and Mare Procellarum, is characterized by K-REE-P (or KREEP) [potassium (K), rare earth elements (REE), and phosphorus (P)] rock, which is enriched in incompatible elements (*2*–*5*). Such material was returned by all Apollo missions (*6*). KREEP-rich material is confined to areas surrounding the Imbrium basin and the Montes Carpatus–Lalande belt (*7*), where the impact deposits provide a datable marker of lunar stratigraphy (*6*, *8*). The age of the Imbrium basin has been inferred from isotope-system shock-resetting data and is debated to be either 3770 or 3850 million years old (*9*, *10*).

Sayh al Uhaymir (SaU) 169 is a 206.45-g rock found in the Sultanate of Oman (*11*). The rock consists of two lithologies (Fig. 1). About 87% by volume (estimates based on tomographic sections) (fig. S1) consists of a holocrystalline, fine-grained polymict impact-melt breccia (stage I in Fig. 1) containing 25 to 40 vol % of shocked rock and mineral clasts. The rock clasts are coarse-grained norites, gabbronorites, and mafic granulites. Crystal clasts comprise plagioclase (An_{57-94}), orthopyroxene ($En_{44-78}Wo_{1-7}$), olivine (Fo_{58-67}), and minor ilmenite, clinopyroxene, spinel, tridymite, or kamacite (table S1). The mineral chemistry of clasts suggests the presence of norites to olivine norites and subordinate, more evolved magmatites (granodiorites to granites) and a few granulites at the impact area. No highland anorthosites ($An_{>97}$) were identified.

The fine-crystalline impact melt (generally <200-μm grain diameter) consists of short-prismatic, low-Ca pyroxene ($En_{61-64}Wo_{3-4}$), mildly shocked plagioclase (An_{75-81}), and potassium feldspar, ilmenite, whitlockite, olivine (Fo_{58-59}), zircon, troilite, kamacite, and tridymite (see also table S1). The impact melt ilmenites contain unusually high Nb_2O_5 (~0.5 wt %), which distinguishes them from known lunar ilmenites (*6*). The impact melt is partially rimmed by shock-lithified regolith (13 vol%). We distinguish two stages of regolith formation (II and III in Fig. 1) from compositional differences. Regolith II and III comprise clasts of crystalline and glassy volcanic rocks, magmatic rocks, breccias, mafic granulites, and crystal fragments. Only stage III regolith is bordered by flow-banded glass and contains yellow and orange glass fragments (including glass beads), olivine basalts, pyroxferroite-bearing basalts, and an anorthosite clast. The basaltic clasts encompass the full range of compositions from Ti-rich to Ti-poor basalts, including aluminous members and picrobasalts (table S2). Glassy shock veins (stage IV in Fig. 1)

[1]Institut für Geologie, Universität Bern, Baltzerstrasse 1, CH-3012 Bern, Switzerland. [2]Naturhistorisches Museum der Burgergemeinde Bern, Bernastrasse 15, CH-3005 Bern, Switzerland. [3]Physikalisches Institut, Abteilung für Weltraumforschung und Planetologie, Universität Bern, Sidlerstrasse 5, CH-3012 Bern, Switzerland. [4]Laboratory for Isotope Geology, Swedish Museum of Natural History, Box 50007, SE-104 05, Stockholm, Sweden. [5]National Science Foundation–Arizona Accelerator Mass Spectrometry Laboratory, University of Arizona, 1118 East Fourth Street, Tucson, AZ 85721, USA. [6]Paul Scherrer Institut, 5232 Villigen, Switzerland. [7]Max-Planck-Institut für Chemie, Abteilung Kosmochemie, 55020 Mainz, Germany. [8]Departement für Chemie und Biochemie, Universität Bern, Freiestrasse 3, CH-3012 Bern, Switzerland. [9]Planetary and Space Sciences Research Institute, Open University, Milton Keynes MK7 6AA, UK.

*To whom correspondence should be addressed: gnos@geo.unibe.ch